HHS Public Access

Author manuscript

Acad Radiol. Author manuscript; available in PMC 2020 March 01.

Published in final edited form as:

Acad Radiol. 2019 March ; 26(3): 367–382. doi:10.1016/j.acra.2018.10.001.

Multi-breath hyperpolarized 3He imaging scheme to measure alveolar oxygen tension and apparent diffusion coefficient

Tahmina Achekzai[1], **Hooman Hamedani**[1], **Stephen J. Kadlecek**[1], **Kai Ruppert**[1], **Yi Xin**[1], **Ryan J. Baron**[1], **Ian F. Duncan**[1], **Federico Sertic**[1], **Sarmad Siddiqui**[1], **Faraz Amzajerdian**[1], **Mehrdad Pourfathi**[1], **Luis A. Loza**[1], **Maurizio Cereda**[2], and **Rahim R. Rizi**[1]

[1]Department of Radiology, University of Pennsylvania, Philadelphia, PA 19104, USA

[2]Department of Anesthesiology and Critical Care, University of Pennsylvania, Philadelphia, PA 19104, USA

Abstract

Rationale and Objective: In this study, we compared a newly developed multi-breath simultaneous alveolar oxygen tension and apparent diffusion coefficient (P_AO_2-ADC) imaging sequence to a single-breath acquisition, with the aim of mitigating the compromising effects of inter-voxel flow and slow-filling regions on single-breath measurements, especially in COPD subjects.

Materials and Methods: Both single-breath and multi-breath simultaneous P_AO_2-ADC imaging schemes were performed on a total of ten human subjects (five asymptomatic smokers and five COPD subjects). Estimated P_AO_2 and ADC values derived from the different sequences were compared both globally and regionally. The distribution of voxels with non-physiological values was also compared between the two schemes.

Results: The multi-breath protocol decreased the ventilation defect volumes by an average of 12.9±6.6%. The multi-breath sequence generated non-physiological P_AO_2 values in 11.0±8.5% fewer voxels than the single-breath sequence. Single-breath P_AO_2 maps also showed more regions with gas-flow artifacts and general signal heterogeneity. On average, the standard deviation of the P_AO_2 distribution was 16.5±7.0% lower using multi-breath P_AO_2-ADC imaging, suggesting a more homogeneous gas distribution. Both mean and standard deviation of the ADC increased significantly from single- to multi-breath imaging (P=0.048 and p=0.070, respectively), suggesting more emphysematous regions in the slow-filling lung.

Conclusion: Multi-breath P_AO_2-ADC imaging provides superior accuracy and efficiency compared to previous imaging protocols. P_AO_2 and ADC maps generated by multi-breath imaging allowed for the qualification of various regions as emphysematous or obstructed which single-breath P_AO_2 maps can only identify as defects. The simultaneous P_AO_2 and ADC measurements

Corresponding Author: Rahim R. Rizi, Hospital of the University of Philadelphia, MRI Learning Center, 3400 Spruce St, 1 Founders Pavilion, Philadelphia, PA 19104, Phone: (215) 615-2426, rahim.rizi@uphs.upenn.edu.

generated by the presented multi-breath method were also more physiologically realistic, and allowed for more detailed analysis of the slow-filling regions characteristic of COPD subjects.

INTRODUCTION

Hyperpolarized (HP) gas magnetic resonance imaging has recently emerged as a technique capable of safely detecting a variety of changes in the lungs such as air flow restriction, airspace enlargement, decreased tissue perfusion, alveolar membrane thickening, and air trapping (1,2), thereby expanding upon the parameters available from conventional modalities like CT and x-ray imaging and enabling the accurate, regional evaluation of gas flow and uptake (3–5).

Two parameters which HP gas MRI is uniquely capable of assessing are regional alveolar oxygen tension (P_AO_2), which reflects oxygen delivery to the parenchyma and uptake into the blood, and apparent diffusion coefficient (ADC), which describes the diffusion of gas within various regions of the lung. Because P_AO_2 reflects the balance between gas replacement through ventilation and uptake into the blood, it is sensitive to early manifestations of chronic obstructive pulmonary disease (COPD), an inflammatory lung condition causing chronic obstruction of airflow. ADC, on the other hand, is primarily indicative of structural changes in alveolar size and connectivity that are expected later in disease progression (6,7). Often acquired simultaneously and coregistered, P_AO_2 and ADC can serve as important indicators of pathophysiological changes in the lungs (8), and together provide a more comprehensive portrait of lung function and structure than is available with other methods—increasing sensitivity to early subclinical alterations and, thereby, diagnostic power (7,9).

Yet previous schemes used for measuring P_AO_2 and ADC in COPD subjects have failed to achieve optimal quality, primarily because the entire airspace of the lung is not filled after a single breath of contrast agent gas (10,11). As a result, slow-filling regions of the lung cannot be studied, and are prematurely labeled as *defects.* Gas distribution also tends to be significantly heterogeneous in single-breath schemes in diseased lung, and the resulting estimations are susceptible to artifacts resulting from inter-voxel flow. Recently published multi-breath imaging schemes (9) have proved useful in mitigating COPD related symptoms that skew the P_AO_2 measurements (10), but still failed to produce optimal signal-to-noise ratios, thus leaving room for improved accuracy, efficiency and technical simplicity.

Here, we present a technique for simultaneously measuring P_AO_2 and ADC after a series of HP ^{3}He wash-ins which incorporates several improvements to previous schemes. Measuring P_AO_2 and ADC during the same breath-hold enables the most efficient use of the polarized gas, while imaging after HP gas wash-in ensures that the whole ventilated lung is imaged with a high and maximally homogenous signal-to-noise ratio. We compare this method with a single-breath scheme using the same pulse sequence during the breath-hold. While several previous papers have discussed various advantages of multi-breath imaging and provided detailed information on gas dynamics, including the volume of administered gas, timing, flow rate, fraction of inhaled oxygen (FiO_2) and end tidal O_2 and CO_2 (EtO_2/CO_2) (10,12,13), these have not addressed simultaneous P_AO_2-ADC imaging schemes. By

performing such a comparison, we will assess the extent to which additional lung volume becomes accessible for analysis and demonstrate that homogenous gas distribution leads to less artifact-prone measurements.

MATERIALS AND METHODS

Demographics

10 subjects were imaged for this study: five asymptomatic nonsmokers (women, n = 3; men, n = 2; age = 62.8 ± 6.1) and five COPD subjects (women, n = 0; men, n = 5; age, 56.4 ± 13.0; GOLD stage IV, n = 2; GOLD stage III, n = 1; GOLD stage I, n = 1; GOLD stage 0, n = 1). Table 1 displays subject demographics, St. George's Respiratory Questionnaire (SGRQ) results, and a subset of pulmonary function test results. All subjects underwent both multi-breath and single-breath combined P_AO_2 imaging in supine position. The two groups were not significantly different with respect to their age, TLC and BMI (refer to Table 1).

Measurement of P_AO_2

P_AO_2 measurements are derived from the longitudinal relaxation rate ($1/T_1$ of HP ^{3}He gas due to interaction with molecular oxygen in vivo, which depends linearly on the oxygen concentration [O_2] (14). In a series of ^{3}He lung images acquired with a low flip angle gradient-echo pulse sequence (GRE), this relationship can be used to calculate the oxygen tension.

P_AO_2 is measured for each voxel by calculating the longitudinal relaxation rate using the following equation (15) and extracting the signal drop of each successive image:

$$\frac{1}{T_1} = 0.45\left(\frac{299}{T}\right)^{0.42}[O_2] \quad \text{(eq. 1)}$$

where T_1, the longitudinal relaxation time, T, body temperature, and [O_2], oxygen concentration, are measured in s, K and Amagat, respectively. At body temperature, eq. 1 yields:

$$T_1 = \frac{E}{P_AO_2} \quad \text{(eq.2)}$$

With $E = 1.95 \times 10^3$ Torr. It is important to note that accurate P_AO_2 measurements require a known relationship between local signal decay and the true (oxygen-induced) T_1 of that gas. Redistribution of inhomogeneous signal during breath-hold, whether through resolution of local pressure gradients or gas diffusion, has the potential to confuse this relationship, generating non-physiological over- or underestimations of P_AO_2, as previously shown (16). It is therefore imperative to begin the breath-hold with the most homogeneous gas distribution possible. Such uniformity is achieved after the end of a series of wash-in breaths, and is coincident with maximum signal intensity. In addition, the series of the short

breath-holds during wash-in can be used to measure regional fractional ventilation (FV) (9,10,17).

The simultaneous acquisition of P_AO_2 and FV was initially designed to correct for the influence of oxygen relaxation on the derived fractional ventilation, as models which do not consider the regional T_1 decay can erroneously interpret changes in signal intensity between breaths as arising from gas replacement by ventilation (18). In order to obtain the most accurate measurements of FV, a longer breath-hold was used to estimate the rate of signal loss during the breathing sequence, simultaneously correcting the FV values. This rate was used to correct the signal buildup between breaths and, using eq. 2, yield the local P_AO_2. As previously shown, the two values can be combined to yield the local rate of oxygen uptake (9).

The model is based on the magnetization to each acquired image *n,* where the ^{3}He magnetization for each nth acquired image can be expressed as below:

$$M_n = M_0 \cos^{n*N_{PE}}(\alpha) \times \exp\left[-\frac{P_AO_2 * t_n(k)}{\xi}\right] \quad \text{(eq.3)}$$

Where M_0 is the initial magnetization level of ^{3}He, N_{PE} is the number of phase-encode gradients for each imaged slice, and α represents the flip angle. $t_n(k)$ is the start time of the nth acquisition for the kth slice.

Although not measured in this study, the proposed scheme is capable of generating values for fractional ventilation (FV), the ratio of gas added to a region in the lung to the volume at end-inspiration. This value is calculated based on the magnetization available after each inhalation, $M_A(j)$.

$$M_A(j) = FV * M_S + (1 - FV) \cdot M_A(j-1) \cdot \exp(D_A),\ M_A(0) = 0 \quad \text{(eq.4)}$$

D_A accounts for all localized relaxation mechanisms, the most significant of which include oxygen-induced relaxation and RF depolarization. Because the reservoir relaxation time significantly exceeds the scan time, ex vivo relaxation in the ^{3}He reservoir can be considered negligible.

Simultaneous measurement of P_AO_2 and ADC

ADC imaging can then be added to this two-parameter sequence (9). As with all implementations, ADC imaging required two acquisitions of each k-space point, with and without matched, bipolar diffusion-encoding gradients. The local ADC value is then defined as:

$$ADC = \frac{1}{b_0}\left(log\frac{S_0}{S_1}\right) \quad \text{(eq.5)}$$

in which S_0/S_1 corresponds to the measured signal intensity without/with diffusion encoding. The parameter b_0 combines the strength and duration of the gradients, as is standard for liquid and gas diffusion measurements by MRI. Although the numerical value of ADC can vary with gradient duration even as b_0 is held constant, we utilize the commonly-chosen standard diffusion pulse timing parameters with no inter-pulse delay (9).

Finally, an additional scan was added to constrain the local flip-angle (14). Although not directly of interest, this value is required to accurately decouple the effects of oxygen-induced signal decay and RF-pulses. Here, we built upon strategies used in previous schemes (20–22) by generalizing their use for multi-slice imaging and eliminating the time delays between the groups of paired acquisitions.

The most efficient image timing—which we employed in this study—uses four images during the breath-hold to constrain the four parameters of interest (overall signal intensity, flip-angle, ADC and P_AO_2). Comparable single-breath schemes (20–22) have also been implemented, and utilize the same acquisition parameters as in this study; paired sets of interleaved 6-slice images are acquired during a 12-s acquisition time, corresponding to four scans of each slice (20). The image timing used here was previously validated by a study comparing four single-acquisition timing schemes with varying inter-scan delay times (20): a “decrease” scheme with inter-scan times becoming shorter as the breath-hold progressed, an “increase” scheme with inter-scan times lengthening over time, an “even” scheme with consistent inter-scan delays, and a “hybrid” scheme in which the first two and last two images were taken close together, while those in between were more spread out. The hybrid scheme was shown to have the least uncertainty in computing both the initial partial pressure of oxygen and the oxygen uptake rate, R. The four-point imaging scheme used here to measure P_AO_2 followed a similar design: the first two time points were taken immediately after one another at the very start of the breath-hold, while the third and fourth time points were taken immediately after one another at the end of the breath-hold. Although Ventilation Defect Volume (VDV) and Ventilation Defect Percentage (VDP) metrics were not calculated for the subjects of this study, when computed the VDV is found by subtracting the ventilation volume from the thoracic cavity volume, and VDP is defined by the ratio of VDV to the thoracic cavity volume. Thoracic cavity volume is based on a thoracic cavity mask obtained by segmenting ^{1}H images.

Imaging Parameters

The complete imaging scheme used here is summarized in Figure 1. All imaging studies used a whole-body 1.5 Tesla (T) MRI scanner (MAGNETOM Sonata, Siemens Medical Solutions, Malvern, PA) with an eight-channel chest coil (Stark Contrast, Erlangen, Germany) tuned to the ^{3}He resonance frequency of 48.48 MHz. One set of diffusion-weighted ADC sequences with interleaved b-values, as well as two back-to-back GRE sequences, were taken on each slice. Six coronal slices were acquired using a GRE pulse-sequence with field of view (FOV) = 40 × 30 cm^2, slice thickness (ST) = 25 mm, interslice gap = 20% ST, flip angle $\alpha_{nominal}$ = 5°, matrix size = 48 × 36 pixels, N_{PE} = 36, repetition time/echo time (TR/TE) = 6.69/3.1 ms. Four images of each of the six coronal slices (A to F) were acquired continuously in an interleaved “AABB…EEFFAABB…EEFF” pattern. 24

raw images were collected in 12 s with 8.3 × 8.3 × 15.6 mm^3 voxel-size resolution. The image pair for each slice utilized interleaved ADC sequences acquired with b = 0 and b = 1.6 cm^2/s. The second image pair was acquired without diffusion-encoding gradients (b = 0) in a non-interleaved manner but with the same TR and TE as the ADC acquisition; the latter pair was primarily used to constrain the flip-angle, and a comparison between early and late b=0 images was used primarily to derive P_AO_2. However, a complete fitting model accounted for both effects in comparing the three signal values.

Imaging Studies

All experimental protocols were approved by the Institutional Review Board at the University of Pennsylvania, and informed subject consent was given. Subjects' vital signs were continuously monitored throughout the imaging session, and a physician supervised the entire procedure. Single and multi-breath imaging schemes were performed on two different days for two of the ten subjects, and back-to-back for the other eight.

For the single-breath protocol, HP ^3He, N_2 and O_2 were mixed at a prescribed ratio of $^3He:N_2:O_2$ = 3:1:1, while the gas ratio was 1:3:1 for the multi-breath schemes (FiO_2 was 21% in both cases).

The volume of administered gas was adjusted to functional residual capacity (FRC) + 12% total lung capacity, which was measured by plethysmography prior to each MRI session. The single-breath P_AO_2 protocol consisted of three breaths of regular air, after which the hyperpolarized gas was administered immediately before the 12-s breath-hold. The multi-breath P_AO_2 protocol included six breaths of imaging gas before the imaging breath-hold; these six breaths prior to imaging take between 30-50 seconds, with a 2-3 sec inhale, 1 sec imaging, and 3-4 sec exhale, for each breath Previous experiments have shown that seven breaths are sufficient to allow for the proper distribution of the HP gas across the lungs while making effective use of the original gas's magnetization (9).

Gas Delivery Device/System

Hyperpolarized ^3He was delivered to subjects over a series of breaths at a set volume and fraction of inspired oxygen (FiO_2) using a custom-built gas delivery device (refer to Figure 2), and image acquisition was synchronized with subjects' breathing pattern. The device uses MRI-compatible, differential pressure pneumatochometers to report the flow rates of gas components, triggering the pneumatic valves and starting the MRI scanner when it reaches the target volume.

Respiratory measurements were also collected using the gas delivery monitoring system designed by Biopac Systems Inc. (USA, California), including data on the percentage of inhaled and exhaled gas as detected by pressure sensors in the gas delivery system. Figure 2 also displays the schematic of the gas delivery system: the subject inhales from and exhales into the mouthpiece, which extends from the breathing valve; the breathing valve also includes a mixed-expired gas port, which detects the gas inhaled and exhaled by the subject. The gas delivery monitoring system, Biopac MP150, which is stored in a separate back room adjacent to the imaging room housing the MRI, is connected to both the exhale and inhale ports. The instrument includes an O_2 and CO_2 analyzer, as well as two flow meters.

It should be noted that the gas port in the breathing valve does not distinguish between exhaled and inhaled gas, although the instantaneous fraction of inhaled oxygen (FiO_2) and end-tidal CO_2 ($EtCO_2$) shown in the gas delivery monitoring data can be used to differentiate inhalation and exhalation portions. Measurements of the volume and duration of breaths, as well as the separate volumes of each breath, were taken for each subject using this system, and any significant deviations from expected values were used to qualify viable data. The volume of inhaled gas is calculated based on the differential pressure drop and measurement of flow, presented and discussed later in figure 9.

HP ^{3}He Production

Imaging gas ($^3He:N_2$ = 99.19:0.81, Linde, Branchburg, NJ) was polarized via the spin-exchange optical pumping method by inducing spin-exchange collisions with optically pumped rubidium atoms using a commercial polarizer (IGI 9600.He, GE Healthcare, Durham, NC).

After 15 hours of optical pumping, polarization reached levels between 25-35%. Hyperpolarized ^{3}He gas was diluted with medical grade 99.999% purity nitrogen gas according to each subject's weight and lung capacity. The mixture of ^{3}He and N_2, stored in a Tedlar bag (Jensen Inert Products, Coral Springs, FL) was combined with a 1L bag of O_2 during administration such that an FiO2 of 21% was maintained throughout the study.

Data Analysis

Data and image analysis was performed using custom software developed in the MATLAB environment (MathWorks, Inc., Natick, Massachusetts, USA). The equation $S = \sqrt{S^2 - \sigma^2}$ was used to bias-correct for background noise in the acquired images, with S representing the signal and σ the inherent background noise. This parameter, σ, was calculated from the average background noise in a 10×10 pixel region, $\bar{B}$, according to the relation, $\sigma = \bar{B}\sqrt{2/\pi}$.

Automatic contrast-limited adaptive histogram equalization (CLAHE) (23) with a gray-scale threshold was used in order to mask the background noise and segment the lung. Because differences in lung position can potentially affect results, a non-rigid demon-based co-registration was performed on spin density maps from all time points before implementing the fitting process. The 2D maps of each slice underwent translation, rotation and scaling, and shearing was set to 0. The CLAHE segmentation technique was performed on both ^{1}H and ^{3}He images, after which a morphology-based co-registration (24) between ^{1}H and ^{3}He (25) was performed. ^{1}H images were taken to obtain general anatomical information on the lung. For P_AO_2 imaging, the images were registered so that three time-points were registered to a fourth one, usually the image with the highest SNR and largest area.

Homogeneity of spin density maps was computed using the properties of gray-level cooccurrence matrix (GLCM), which is an m-by-n-by-p array of valid gray-level for extracting second-order features of an image and represents the specified spatial relationship between pixels (26). Each element (r,c) in the normalized GLCM is the joint probability occurrence of pixel pairs with a defined spatial relationship having gray level values r and c

in the image. 'Homogeneity' is defined by a value that measures the closeness of the distribution of elements in the GLCM to the GLCM diagonal (27) as below:

$$Homogeneity = \sum_{i,j} \frac{p(i,j)}{1 + |i - j|} \quad \text{(eq.6)}$$

Statistical Analyses

All statistical analyses were performed using R software, an open-source project distributed under the GNU General Public License (Copyright 2007 Free Software Foundation, Inc.). Paired t-tests were performed to compare different parameters of single- and multi-breath imaging. An experiment-wide Type I error level of 0.05 was used.

For hybrid acquisition schemes, all validation/confirmation tests were performed at the global level (whole lung sum of signal), whereas all other statistical comparisons were performed at the voxel, slice, or region of interest (ROI) level in order to maintain the regionality of the data. Data are presented as the mean and standard deviation.

RESULTS/DISCUSSION

In this study, we presented an updated method for simultaneously imaging two lung function parameters, P_AO_2 and ADC, which we successfully performed on both asymptomatic smokers and COPD subjects using a multi-breath protocol in an effort to best replicate physiological breathing and maximize gas distribution. The presented scheme increases the volume of lung available for analysis, as regions that remain unventilated under a single-breath imaging scheme are filled with gas after the six short breaths incorporated into the multi-breath procedure. In addition to the expanded lung volume it makes available for analysis, the multi-breath scheme also homogenized gas distribution, equilibrating signal across the lung and eliminating many of the non-physiological measurements and artifacts that result from inter-voxel flow during single-breath imaging.

Though a multi-breath scheme produces more accurate P_AO_2 and ADC values, it does so at the cost of signal-to-noise: a quick inhalation of the full volume of anoxic gas in a single breath yields approximately twice the signal-to-noise available after the last inhalation in a seven-breath breathing sequence. To ameliorate the issue of low SNR that accompanies multi-breath imaging, the method presented here incorporates a modified pulse sequence from previously-presented hybrid scheme (10). While this previous method relied on two images taken at the beginning of the long breath-hold at low-resolution for a coarse B_1-correction, the last two time-points in the new, updated sequence (refer to Figure 1) and the ADC (b_0=0) are sufficient to decouple the effect of RF- and oxygen relaxations. The improved signal-to-noise ratios still fall short of those achieved with a single-breath method, however, meaning that the presented multi-breath scheme is only practical under conditions of sufficient signal intensity, thereby ruling out the very highest resolution imaging. Nevertheless, because diagnostically relevant functional compromise occurs at the acinar level or above, modest resolution is sufficient to provide a useful, multi-parametric assessment of the lung under physiologically relevant conditions. As this paper shows, such

assessment highlights key abnormalities in lung function critical to COPD diagnosis and tracking, eliminates many of the non-physiological measurements obtained in single-breath imaging, and enables the study of otherwise inaccessible regions of the lung.

Figure 3 depicts the spin density maps obtained from two representative subjects during simultaneous P_AO_2-ADC single-breath imaging (top row for each subject), as well as and during the last time-point (seventh breath) of multi-breath imaging (bottom row) highlighting some of the findings of this study. A qualitative comparison of the two image sets reveals voids in the single-breath images that fill with imaging gas on subsequent breaths—often appearing indistinguishable from nearby, fully ventilated regions (refer to the yellow arrows)—alongside regions that remain devoid of signal. Several relatively large, slow-filling regions are thus shown to retain some function, despite potentially suffering from air trapping or becoming filled through collateral pathways or even recruitment. By allowing the gas enough time to fill those regions, the multi-breath method enables the study of gas dynamics and the quantification of functional parameters like FV, P_AO_2 ADC and uptake in these regions, which was not possible under the single-breath protocol due to absence of signal.

Figure 4 shows the results of fitting eq. 3 and 5 to the signal intensity maps acquired during breath-hold in another representative subject to yield regional maps of P_AO_2 (top) and ADC (bottom), alongside histograms for the six slices covering the whole-lung from anterior to posterior. Both single- and multi-breath P_AO_2 and ADC maps show similar features in most voxels. The overall P_AO_2 was 114±39 Torr versus 90±33 Torr for single- and multi-breath, respectively, while ADC was 0.328±0.107 cm^2/s versus 0.329±0.124 cm^2/s. Gravitational gradients are clearly evident, with both P_AO_2 and ADC values increasing from anterior to posterior slices. Other qualitative features apparent in these maps include the correspondence between regions of elevated ADC and low oxygen tension (yellow arrows) in slow-filling regions that are commonly labeled as ‘defect’ in a single-breath scheme, suggesting regional emphysematous remodeling with associated poor oxygen transport due to either reduced perfusion or poor gas permeability of the alveolar membrane. Table 2 summarizes the resulting imaging markers (mean and standard deviation) for all subjects (P_AO_2-imaging comparison failed for two AS subjects).

Figure 5 shows the parametric maps for four additional subjects, all of whom display larger and more numerous regions of ventilation defect after a single-breath than after multi-breath gas administration. The extent of ventilation defects after a single breath is often assessed in aggregate using Ventilation Defect Percentage (VDP) or Ventilation Defect Volume (VDV) (25)— metrics that do differentiate clearly between healthy and COPD subjects (8,25,28,29), but cannot distinguish between regions that are completely unventilated and those that retain function to some extent (10,11). VDP values are progressively reduced with successive wash-in breaths over the course of a multi-breath series, although some defects remain in diseased subjects even after seven wash-in breaths of imaging gas. Analyzing ventilation defects after multi-breath wash-ins could likely result in a loss of diagnostic sensitivity based on VDP due to this rise of signal in the slow-filling regions in most subjects. Nevertheless, the more comprehensive parameter of fractional ventilation (FV) measurements can be typically employed with multi-breath imaging. In addition, the more

homogeneous gas concentration achieved at the end of the multi-breath maneuver maximizes both the volume accessible to subsequent P_AO_2 and ADC imaging and the accuracy of those images. The defects can also be identified even in multi-breath imaging, by using the images taken after each of the first six breath holds, particularly the first few breaths, before gas does flow into the slow-filling regions. A fit to the signal build-up can provide a more comprehensive measure of ventilation.

Figure 3 also displays examples of inhomogeneous ventilation and its resolution in the multi-breath regime (highlighted by the green arrows), illustrating the potential for single-breath imaging to produce inaccurate parametric maps. To the extent that these scattered patches of high and low intensity are equilibrated during the breath-hold, erroneous T_1 (and, by extension, P_AO_2) values will be attributed to the corresponding regions. Ensuring equilibration before the beginning of the P_AO_2 measurement greatly reduces this artifact (10,12). The correlation plots in Figure 6A demonstrate this effect across the whole cohort, which show a strong negative relationship between a homogenous initial signal distribution and the number of non-physiological P_AO_2 voxel values (refer to Table 2) present in a subject's P_AO_2 map; the correlation shows a goodness-of-fit value of −0.886. Because they are inconsistent with the inhaled gas mixture or with respiratory physiology, these non-physiological values (P_AO_2 > FiO2 or P_AO_2 < 40mmHg) represent the degree of artifact present in the image (Figure 6A, left). The overall inhomogeneity of the P_AO_2 map is reduced as well (Figure 6A, right), although with a slightly weaker correlation, with a goodness-of-fit parameter of −0.731, likely because the analysis is not restricted to voxels known to display erroneous values. When directly comparing the difference in the number of non-physiological voxels or the width of the P_AO_2 distribution after single and multiple breaths, we find that the latter administration scheme results in a 11.0±8.5% (maximum of 25%, $p = 0.008$) and 16.5±7.0% (maximum of 27%, $p < 0.001$) reduction, respectively. In demonstrating that the reduced signal inhomogeneity (Figure 6B) achieved through the multi-breath maneuver largely ameliorates image artifacts (Figure 3), we have provided strong evidence that multi-breath imaging produces superior parametric maps.

In addition to more homogeneous P_AO_2 values, multi-breath imaging increases the volume accessible for analysis by an average of 12.9±6.6% (maximum of 24.7%,) for all subjects, as summarized in Table 3 and illustrated in Figure 7. Two representative subjects illustrate the fact that these newly-accessible regions have a somewhat different character than those that are well-ventilated on the first breath: for example, both ADC mean and heterogeneity in all subjects were marginally higher with multi-breath administration compared to single-breath (P=0.048 and P=0.070, respectively), showing that the slow-filling regions were typically more emphysematous (COPD 5 being an exception). In regions of the lungs displaying signal under both administration techniques, ADC measurements showed no detectable bias or other significant differences.

On the other hand, the reduced tendency toward artifacts noted above did result in noticeably different P_AO_2 measurements: even in regions accessible by both protocols, P_AO_2 values fell into the physiological range (40 Torr < P_AO_2 < FiO2) more frequently in the multi-breath method. The similarity between single- and multi-breath ADC is due to the fact that the multi-slice acquisition is too fast for noticeable macroscopic gas flow to occur. Thus, while

multi-breath imaging produces more voxels, inter-voxel redistribution does not skew the results to the same extent that it does for P_AO_2, for which imaging time is several seconds. Both lower and higher than normal P_AO_2 values were observed in the regions newly accessible to multi-breath imaging, which can be related to different perfusion alterations in these poorly ventilated regions.

In subjects who followed the entire protocol correctly, the improvement between single- and multi-breath imaging is readily apparent, with the latter enabling a more complete examination of the diseased lung. This improvement is summarized in Figures 8, in which, despite the reduced maximum signal-to-noise in the P_AO_2/ADC image set, the greater gas volume in the lung provides sufficient signal for the accurate quantification of both. Figure 8 displays histograms of the distributions of P_AO_2 and ADC values in single- and multi-breath imaging. In the P_AO_2 distribution plots especially, the plots are narrower in the multi-breath protocol; this decrease in standard deviation indicates that the P_AO_2 measurements are more similar to each other, and the maps more homogeneous, in the multi-breath protocol. There are therefore fewer artifacts on either extremity of P_AO_2 measurements, which results in more physiological measurements. In that the distributions are narrowed despite a lower initial signal-to-noise, we can be certain that ameliorating these inter-voxel flow effects has more impact on the parametric map accuracy than the higher signals associated with the single-breath administration.

The reliability of parametric maps can be further evaluated and improved using ancillary measurements of global breathing dynamics. Even very small accidental inhalations or exhalations during the breath-hold can skew the results of any imaging parameters in which the voxel's gas is assumed to be stationary during imaging acquisition. P_AO_2 maps are particularly susceptible to subject non-compliance, as the addition or removal of contrast agent gas masks the true extent of oxygen-induced T_1. In this dataset, we have employed two methods to validate our measurements, as exemplified in Figure 9. The first (9A) is by comparing lung volume at the beginning and end of the breath-hold; differences above a predefined threshold, in our case 5% of lung volume at the beginning of the breath-hold, indicate significant subject motion or inhalation/exhalation that will skew the results. In addition, the breathing device monitors subject compliance by measuring airflow during what is nominally the quiescent breath-hold duration (9B, top trace). In this representative case, easily detectable exhalation (9B, 2nd row; orange arrow), coupled with a lung volume decrease of 33.6%, indicates a failed breath-hold. The P_AO_2 values from this subject (AS2) were therefore excluded, as were those from AS5, on the same basis but due to intermittent small inhalations (9B, 2nd row; red arrow). Because ADC measurements involve comparison between measurements acquired only a few ms apart (interleaved k-space coverage), sensitivity to gas flow and subject motion is minimal; the ADC values from these two subjects are therefore included in the analysis.

The remaining traces on Figure 9B indicate continuous measurements of O_2 and CO_2 concentration, which provide an additional verification of FiO_2, EtO_2 and $EtCO_2$. Figure 10 shows the correlation between the EtO_2 and $EtCO_2$ with estimated global values for P_AO_2, with a good agreement between the global measures of imaged alveolar oxygen tension and the expired gas analysis. Single-breath P_AO_2 measurements were derived from the ETO_2

and $ETCO_2$ after the first breath, while multi-breath P_AO_2 measurements used the ETO_2 and $ETCO_2$ from the last time-point breath. Both the wide range and bias observed between single- and multi-breath images is the result of different EtO_2 ranges for the first and last breath in different subjects.

LIMITATIONS

Several aspects of both the gas delivery method and the image analysis portion of this study contributed to potential variations in its findings. Certain aspects of gas delivery are out of the experimenters' control, as subjects' breathing patterns are not entirely consistent from one experiment to the next, and cannot be made so without mechanical ventilation.

As mentioned above, two subjects' data was rejected from the final set analyzed because of a failure to comply with the breathing scheme. One of these subjects consistently took a small breath in the middle of scheduled breath-holds while the other one exhaled during the breath-hold, thereby skewing their P_AO_2 results. It is also true that subjects do not inhale and exhale equal amounts of air with each breath, nor do they breathe at entirely consistent rates. Thus, while images are supposed to be taken at FRC + Tidal Volume, it can be impossible to do so when subjects exhale at a volume smaller or greater than a set-point. Fortunately the availability of breathing curves that detect the exhaled and inhaled volumes allows us to determine what time points the images are taken and to correct for that variation accordingly.

The amount of the effective dead-volume in the lung also differs across subjects depending on their demographics and measurements: the ratio of the dead- to tidal-volume is based on height, weight and total lung capacity of the subject. In cases where the combined anatomical and device dead-volume is high compared to tidal volume—for example, in tall, thin subjects with small lungs—the subject may not inhale the proper amount of fresh gas with every breath, since the exhaled gas from the previous breath may be left in the dead volumes. In these cases, we observe the EtO_2 gradually decreasing with every breath at a rate that is not reflective of their lungs' perfusion capacity or diffusion rates (Refer to Figure 9B, EtO_2 gas analysis). For example, Subject COPD 1 had a total lung capacity of 3.7 Liters (tidal volume 450 ml), and a height of 63 inches (anatomical dead space = ~120ml (30)); with a constant gas delivery dead space of 100 ml, the subject rebreathed almost half of the exhaled gas every time, causing a gradual drop in EtO_2 during the breathing sequence (refer to the O_2 graphs on Figure 9B).

Though multi- and single-breath imaging was conducted on all subjects studied, the imaging sessions were not always held on the same day. For two subjects, COPD5 and AS1, multi- and single-breath imaging were conducted on separate days. A previous study demonstrated that more time in between imaging sessions increased variability in the measured P_AO_2 values (31). In these two subjects, then, the differences in range and standard deviation between single- and multi-breath P_AO_2 maps may arise from the disparity in the time of imaging rather than the differences in administration methods.

Some errors may also have arisen during the image analysis process, as lung images must be registered to one another in order to perform regional comparisons between slices in the

same subject, or between one subject and another. However, because subjects do not stay completely still during the study, slight movement can prevent lung images from lining up with one another. This means that the analyzed regions or voxels are not identically matched when comparing the two imaging methodologies, limiting the apparent correlation between the two techniques even under ideal circumstances. Although a smaller effect because all images are acquired during the same breath hold, misregistration may also occur among the images that determine the P_AO_2 maps; extreme versions of this limitation led to rejection of two of the datasets, but smaller motions may lead to artifacts as well, particularly in regions of high signal inhomogeneity.

It is important to note that the field of hyperpolarized gas imaging is transitioning from Helium to Xenon. This transition does suggest there will be some differences in the application of our study to future gas imaging studies. For example, Xenon does provide considerable more information than Helium, distinguishing between gas phase and dissolved phase, and between that dissolved in parenchymal tissue or red blood cells. Xenon imaging can potentially cause an over-estimation of PAO2 that results from the loss of some of the gas signal to dissolved phase. The dissolved phase Xenon makes up about 2% of total inhaled Xe – a statistic calculated by considering parenchyma-gas partition coefficient, 0.1, and the percentage of lung made up by parenchyma, about 20% (32). This uptake, while small, needs to be corrected for when calculating the PAO2 parameter. The dissolved Xe causes a small amount of signal loss, which if not recognized as dissolved-phase Xe, would cause an overestimation of PAO2. However, if incorporated into the fitting model, this loss can be corrected for, generating accurate PAO2 values.

Yet, because Xenon imaging is capable of measuring several other parameters that provide arguably more information than PAO2, PAO2 becomes less critical as a stand-alone measurement. In that case, the use of PAO2 is more relevant in correcting for FV. PAO2 measurements are often more relevant when incorporated with FV, as it can be used to correct for FV measurements. Regional T_1 decay caused by oxygen relaxation can be mistaken for gas replacement by ventilation. Including PAO2 in this model can help distinguish between the signal changes caused by oxygen relaxation and that caused by ventilation.

CONCLUSIONS

We identified several advantages of our newly-presented multi-breath P_AO_2-ADC imaging scheme over the previously-demonstrated single-breath scheme. The multi-breath maneuver requires approximately one more minute of imaging time and no additional gas, but yields considerably more information, including measurements of P_AO_2, ADC, and FV in otherwise unexplored regions. Though FV was not reported in this study, it can be measured from the first six breaths in the multi breath scheme according to (10). Considering the technical complexity and substantial set-up associated with even the simplest hyperpolarized gas studies, we believe that the additional time and instrumentation needed to adapt to a multi-breath approach does not pose a significant impediment to the experimental procedures.

Obtaining the ADC and P_AO_2 values in the same breath-hold also ensures that the measurements are taken under conditions as physiologically similar as possible. The inclusion of the six breaths before the long breath-hold mimics physiological breathing, thereby contributing to a more accurate and realistic reflection of lung function. Taking measurements after the breath-holds also makes them more robust by allowing the magnetization to become more homogenized. We showed that the increased homogenization correlates with more physiological P_AO_2 values.

The ability to generate several parameters under the same protocol allows us to produce multi-parametric maps, which provide a particularly comprehensive picture of lung efficiency and are especially useful when conducting longitudinal or pre-post studies, as they can be utilized to study different regions of the lung over time. Conditions suggested by a pattern in one parameter can be confirmed by a corroborating trend in another, thereby helping to validate any clinical conclusions drawn from earlier imaging sessions. Unlike single-breath P_AO_2-ADC imaging, which labels more abnormalities as ventilation defects, our multi-breath P_AO_2-ADC scheme generates more specific information about such ‘defects’, confirming their presence in some regions while also recognizing those subject to slow-filling and/or collateral ventilation. This could be particularly useful in clinical settings, especially to optimize pulmonary treatment procedures like lung reduction volume surgery (33) or bronchial thermoplasty (34). The generated parameters and qualitative study of images can also prove useful in phenotyping for regional evaluation of disease severity and progression (35).

ACKNOWLEDGMENTS

This work was supported by the National Institutes of Health (NIH) RO1-HL127969.

REFERENCES

1. Galbán CJ, Han MK, Boes JL, et al. Computed tomography-based biomarker provides unique signature for diagnosis of COPD phenotypes and disease progression. Nat Med. 2012; 18(11): 1711–1715. [PubMed: 23042237]
2. Thurlbeck WM, Simon G. Radiographic appearance of the chest in emphysema. AJR Am J Roentgenol. 1978;130(3):429–440. [PubMed: 415543]
3. Kumar S, Liney G, Rai R, Holloway L, Moses D, Vinod SK. Magnetic resonance imaging in lung: a review of its potential for radiotherapy. Br J Radiol. 2016;89(1060)https://www.ncbi.nlm.nih.gov/pmc/articles/PMC4846194/. Accessed July 6, 2018.
4. Mathews JD, Forsythe AV, Brady Z, et al. Cancer risk in 680 000 people exposed to computed tomography scans in childhood or adolescence: data linkage study of 11 million Australians. BMJ. 2013;346:f2360. [PubMed: 23694687]
5. Inaba Y, Chida K, Kobayashi R, Zuguchi M. A cross-sectional study of the radiation dose and image quality of X-ray equipment used in IVR. J Appl Clin Med Phys. 2016;17(4):391–401.
6. Currie GP. ABC of COPD, 3rd Edition 3rd ed. Wiley-Blackwell; 2017https://www.wiley.com/en-us/ABC+of+COPD%2C+3rd+Edition-p-9781119212850. Accessed February 28, 2018.
7. Punturieri A, Croxton TL, Weinmann GG, Kiley JP. Chronic obstructive pulmonary disease: a view from the NHLBI. Am J Respir Crit Care Med. 2008;178(5):441–443. [PubMed: 18713849]
8. Hamedani H, Kadlecek SJ, Ishii M, et al. Alterations of regional alveolar oxygen tension in asymptomatic current smokers: assessment with hyperpolarized (3)He MR imaging. Radiology. 2015;274(2): 585–596. [PubMed: 25322340]

9. Hamedani H, Kadlecek S, Xin Y, et al. A hybrid multibreath wash-in wash-out lung function quantification scheme in human subjects using hyperpolarized3He MRI for simultaneous assessment of specific ventilation, alveolar oxygen tension, oxygen uptake, and air trapping. Magn Reson Med. 2017;78(2):611–624. [PubMed: 27734519]
10. Hamedani H, Clapp JT, Kadlecek SJ, et al. Regional Fractional Ventilation by Using Multibreath Wash-in (3)He MR Imaging. Radiology. 2016;279(3):917–924. [PubMed: 26785042]
11. Marshall H, Deppe MH, Parra-Robles J, et al. Direct visualisation of collateral ventilation in COPD with hyperpolarised gas MRI. Thorax. 2012;67(7):613–617. [PubMed: 22286930]
12. Horn FC, Rao M, Stewart NJ, Wild JM. Multiple breath washout of hyperpolarized 129Xe and 3He in human lungs with three-dimensional balanced steady-state free-precession imaging. Magn Reson Med. 2017;77(6):2288–2295. [PubMed: 27404992]
13. Kruger SJ, Nagle SK, Couch MJ, Ohno Y, Albert M, Fain SB. Functional imaging of the lungs with gas agents. J Magn Reson Imaging JMRI. 2016;43(2):295–315. [PubMed: 26218920]
14. Saam null, Happer null, Middleton null. Nuclear relaxation of 3He in the presence of O2. Phys Rev At Mol Opt Phys. 1995;52(1):862–865.
15. Cereda M, Xin Y, Hamedani H, et al. Mild loss of lung aeration augments stretch in healthy lung regions. J Appl Physiol Bethesda Md 1985. 2016;120(4):444–454.
16. Clapp J, Hamedani H, Kadlecek S, et al. Multibreath alveolar oxygen tension imaging. Magn Reson Med. 2016;76(4): 1092–1101. [PubMed: 26467179]
17. Emami K, Hamedani H, Han B, Kadlecek S, Xu Y, Rizi RR. Automatic Respiratory Gas Delivery Device For Noninvasive Administration Of Hyperpolarized Gaseous Contrast Agents To Consciously Breathing Subjects. American Thoracic Society; 2012 p. A2045–A2045 http://www.atsjournals.org/doi/abs/10.1164/ajrccm-conference.2012.185.1_MeetingAbstracts.A2045. Accessed July 6, 2018.
18. Effect of T 1 relaxation on ventilation mapping using hyperpolarized 129 Xe multiple breath wash-out imaging, https://www.readbyqxmd.com/read/30009427/effect-of-t-1-relaxation-on-ventilation-mapping-using-hyperpolarized-129-xe-multiple-breath-wash-out-imaging. Accessed July 20, 2018.
19. Hamedani H, Kadlecek SJ, Emami K, et al. A multislice single breath-hold scheme for imaging alveolar oxygen tension in humans. Magn Reson Med. 2012;67(5): 1332–1345. [PubMed: 22190347]
20. Yu J, Rajaei S, Ishii M, et al. Measurement of pulmonary partial pressure of oxygen and oxygen depletion rate with hyperpolarized helium-3 MRI: a preliminary reproducibility study on pig model. Acad Radiol. 2008;15(6):702–712. [PubMed: 18486007]
21. Fischer MC, Spector ZZ, Ishii M, et al. Single-acquisition sequence for the measurement of oxygen partial pressure by hyperpolarized gas MRI. Magn Reson Med. 2004;52(4):766–773. [PubMed: 15389934]
22. Fischer MC, Kadlecek S, Yu J, et al. Measurements of regional alveolar oxygen pressure using hyperpolarized 3He MRI. Acad Radiol. 2005;12(11): 1430–1439. [PubMed: 16253855]
23. Reza AM. Realization of the Contrast Limited Adaptive Histogram Equalization (CLAHE) for Real-Time Image Enhancement. J VLSI Signal Process Syst Signal Image Video Technol. 2004;38(1):35–44.
24. Bricault I A fast morphology-based registration CVRMed-MRCAS97. Springer, Berlin, Heidelberg; 1997 p. 417–426 https://link.springer.com/chapter/10.1007/BFb0029264. Accessed July 6, 2018.
25. Kirby M, Pike D, Coxson HO, McCormack DG, Parraga G. Hyperpolarized (3)He ventilation defects used to predict pulmonary exacerbations in mild to moderate chronic obstructive pulmonary disease. Radiology. 2014;273(3):887–896. [PubMed: 24960283]
26. Badrul M, Akter K, Akter A. Detection of Brain Cancer from MRI Images using Neural Network. Int J Appl Inf Syst. 2016; 10(5):6–11.
27. Somwanshi DK, Goswami A. Detection of Abnormalities in MRI Images using Texture Analysis. J Int Acad Phys Sci. 2011;15(0) http://www.iaps.org.in/journal/index.php/journaliaps/article/view/212. Accessed July 20, 2018.

28. Fain SB, Panth SR, Evans MD, et al. Early Emphysematous Changes in Asymptomatic Smokers: Detection with 3He MR Imaging. Radiology. 2006;239(3):875–883. [PubMed: 16714465]
29. Sheikh K, Capaldi DPI, Hoover DA, Palma DA, Yaremko BP, Parraga G. Magnetic resonance imaging biomarkers of chronic obstructive pulmonary disease prior to radiation therapy for non-small cell lung cancer. Eur J Radiol Open. 2015;2:81–89. [PubMed: 26937440]
30. Hart MC, Orzalesi MM, Cook CD. Relation between anatomic respiratory dead space and body size and lung volume. J Appl Physiol. 1963;18(3):519–522. [PubMed: 31094493]
31. Hamedani H, Kadlecek SJ, Ishii M, et al. A variability study of regional alveolar oxygen tension measurement in humans using hyperpolarized 3He MRI. Magn Reson Med. 70(6): 1557–1566.
32. Goto T, Suwa K, Uezono S, Ichinose F, Uchiyama M, Morita S. The blood-gas partition coefficient of xenon may be lower than generally accepted. Br J Anaesth. 1998;80(2):255–256. [PubMed: 9602599]
33. Group NETTR. A Randomized Trial Comparing Lung-Volume–Reduction Surgery with Medical Therapy for Severe Emphysema. 10.1056/NEJMoa030287. 2009 https://www.nejm.org/doi/10.1056/NEJMoa030287?url_ver=Z39.88-2003&rfr_id=ori%3Arid%3Acrossref.org&rfr_dat=cr_pub%3Dwww.ncbi.nlm.nih.gov. Accessed July 27, 2018.
34. Thomen RP, Sheshadri A, Quirk JD, et al. Regional Ventilation Changes in Severe Asthma after Bronchial Thermoplasty with ^{3} He MR Imaging and CT. Radiology. 2015;274(1):250–259. [PubMed: 25144646]
35. Han MK, Kazerooni EA, Lynch DA, et al. Chronic Obstructive Pulmonary Disease Exacerbations in the COPDGene Study: Associated Radiologic Phenotypes. Radiology. 2011;261(1):274–282. [PubMed: 21788524]

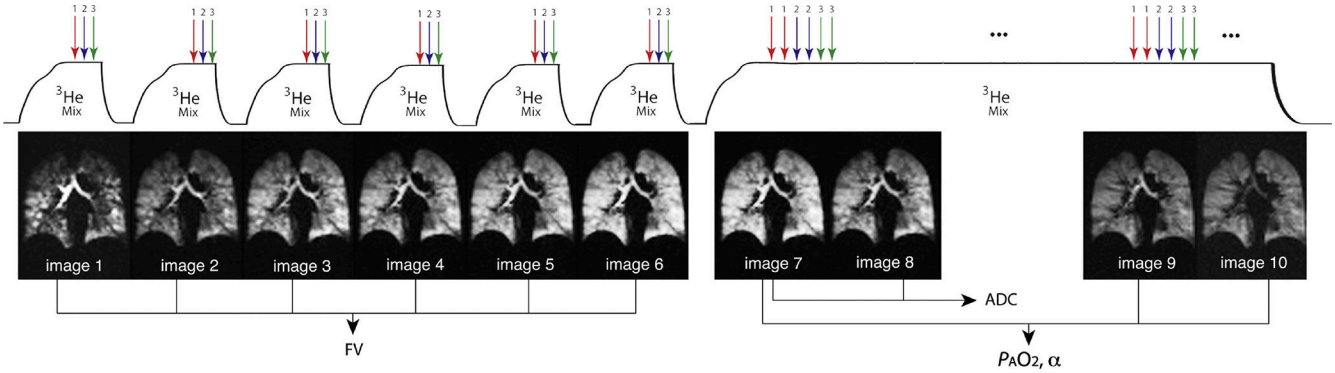

Figure 1).

Newly-presented multi-breath sequence designed to generate measurements of alveolar O_2 tension and gas diffusion. Each slice uses a set of ADC with two interleaved b-values as well as one set of slice-interleaved GRE in a “AABB…EEFFAABB…EEFF” pattern. The ADC image with b_0=0 for each slice and the two last back-to-back interleaved GRE images are sufficient for P_AO_2 calculations (three time-point to decouple flip angle depolarization and oxygen relaxation).

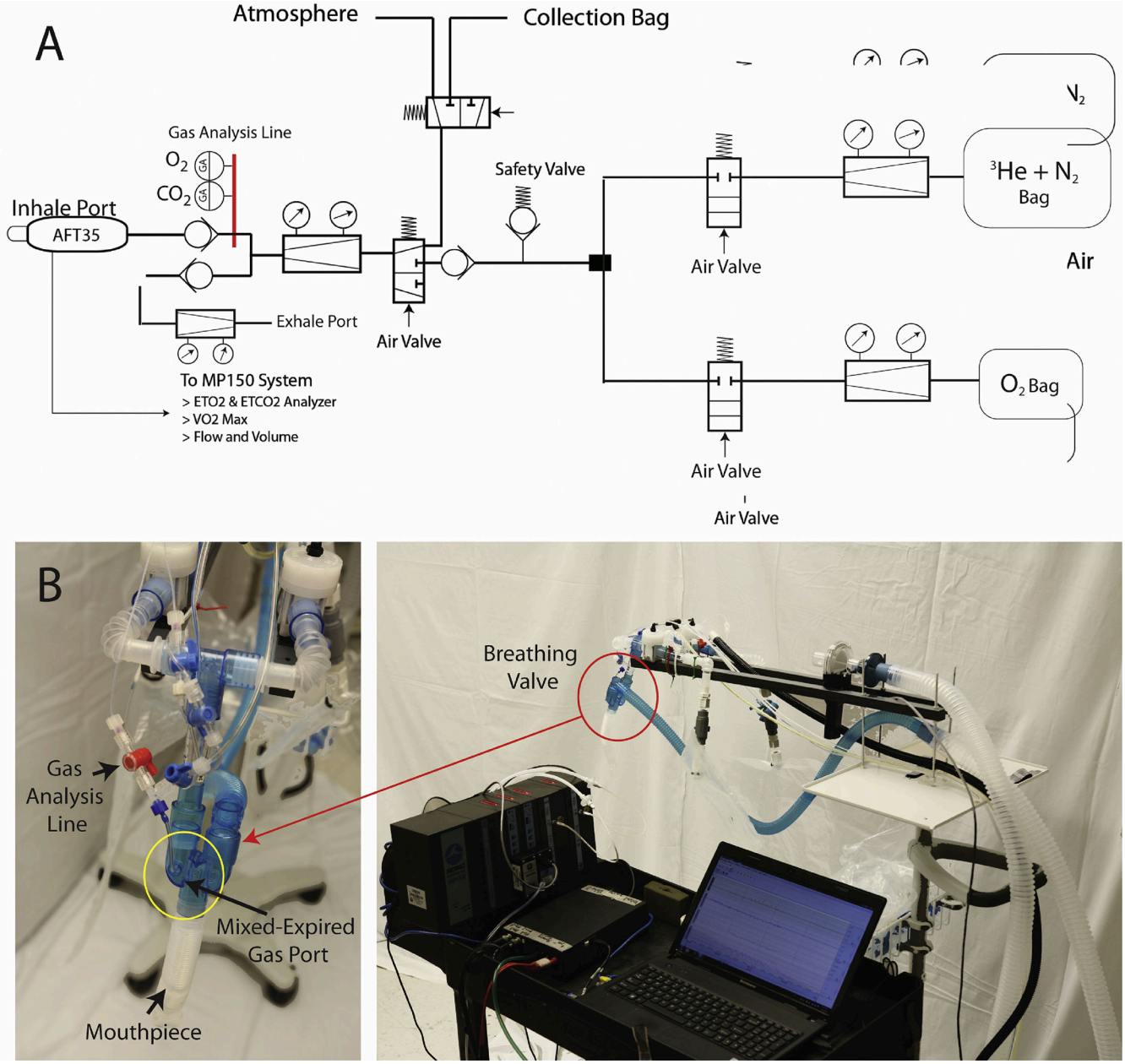

Figure 2).

A: Gas delivery device piping and instrumentation diagram. **B:** Gas delivery prototype and Biopac MP150 instrumentation set-up used in the study.

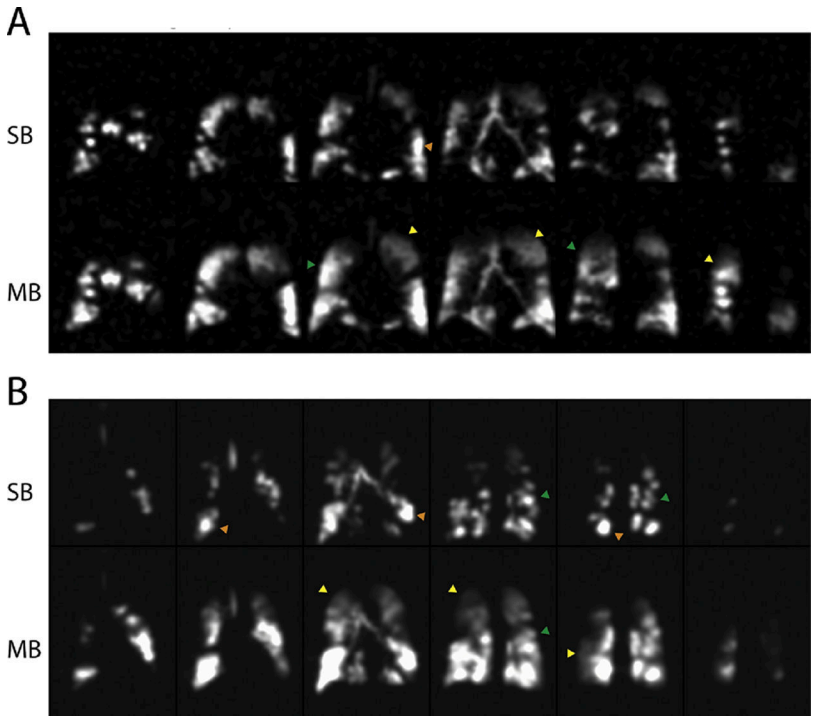

Figure 3).

Spin density maps obtained from representative COPD subjects COPD 1: Age: 70 yrs.; BMI: 27.2; FEV1/FVC: 0.35; DLCO: 37% Pred; RV/TLC: 62% (A) and COPD 5: Age: 61 yrs.; BMI: 23.7; FEV1/FVC: 0.49; DLCO: 51% Pred.; RV/TLC: 59% (B); including both single-breath images (top) and last time-point (7^{th} breath) multi-breath images (bottom). Yellow arrows indicate slow filling regions of the lung where signal intensity is greater in the hybrid multi-breath imaging than in single-breathing imaging; orange arrows indicate regions of over-inflation; green arrows indicate regions where signal homogeneity is improved in the multibreath imaging scheme.

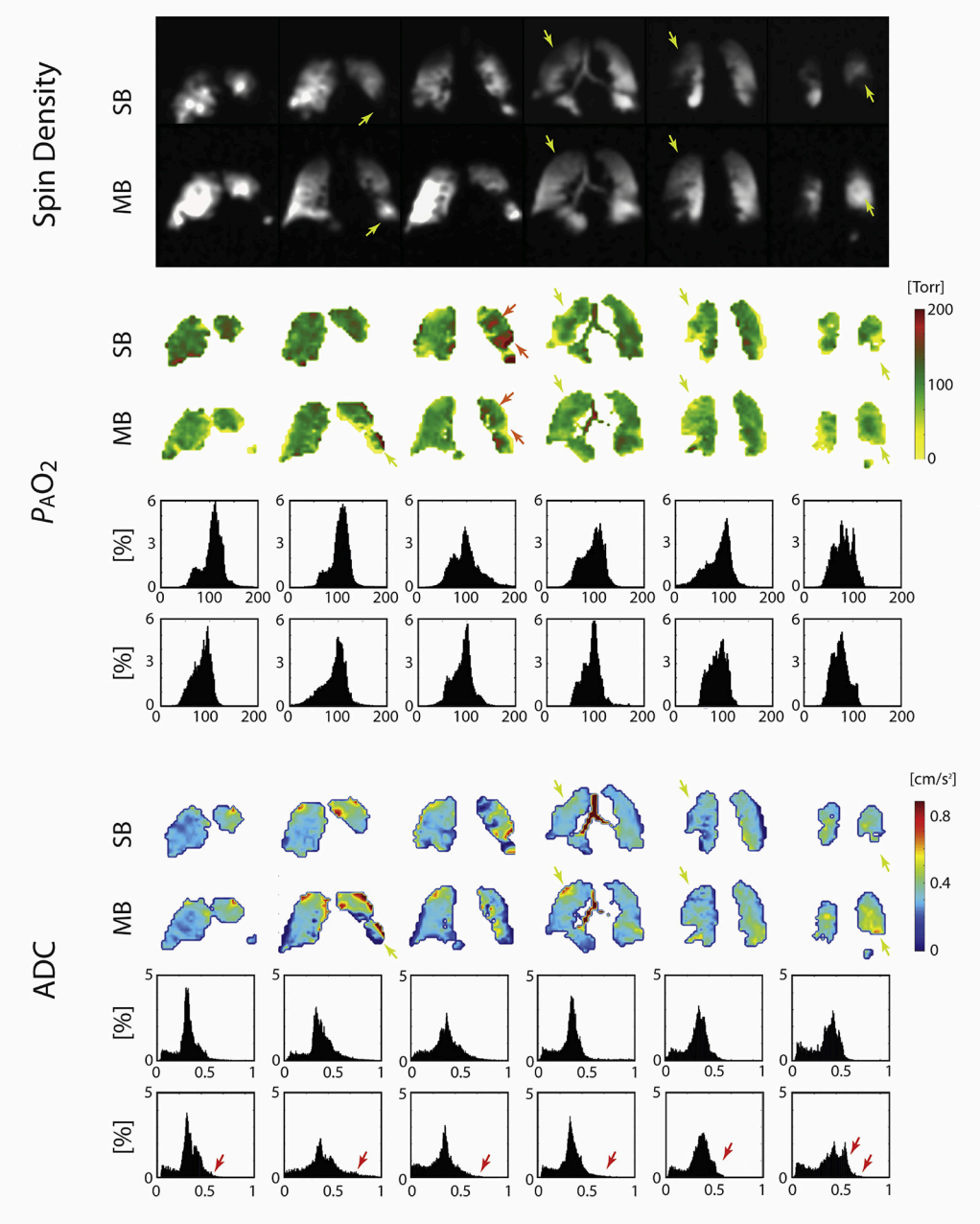

Figure 4).

Maps for subject COPD 3: Age: 60 yrs.; BMI: 27.9; FEV1/FVC: 40%; DLCO: 59% Pred. **Top:** Spin density maps of single- and multi-breath schemes in representative subject COPD3. **Middle:** PAO2 maps and histogram distributions of PAO2 value versus percent incidence in the lungs. **Bottom:** ADC maps and histogram distribution of ADC value versus percent incidence in the lungs in representative subject COPD 3.

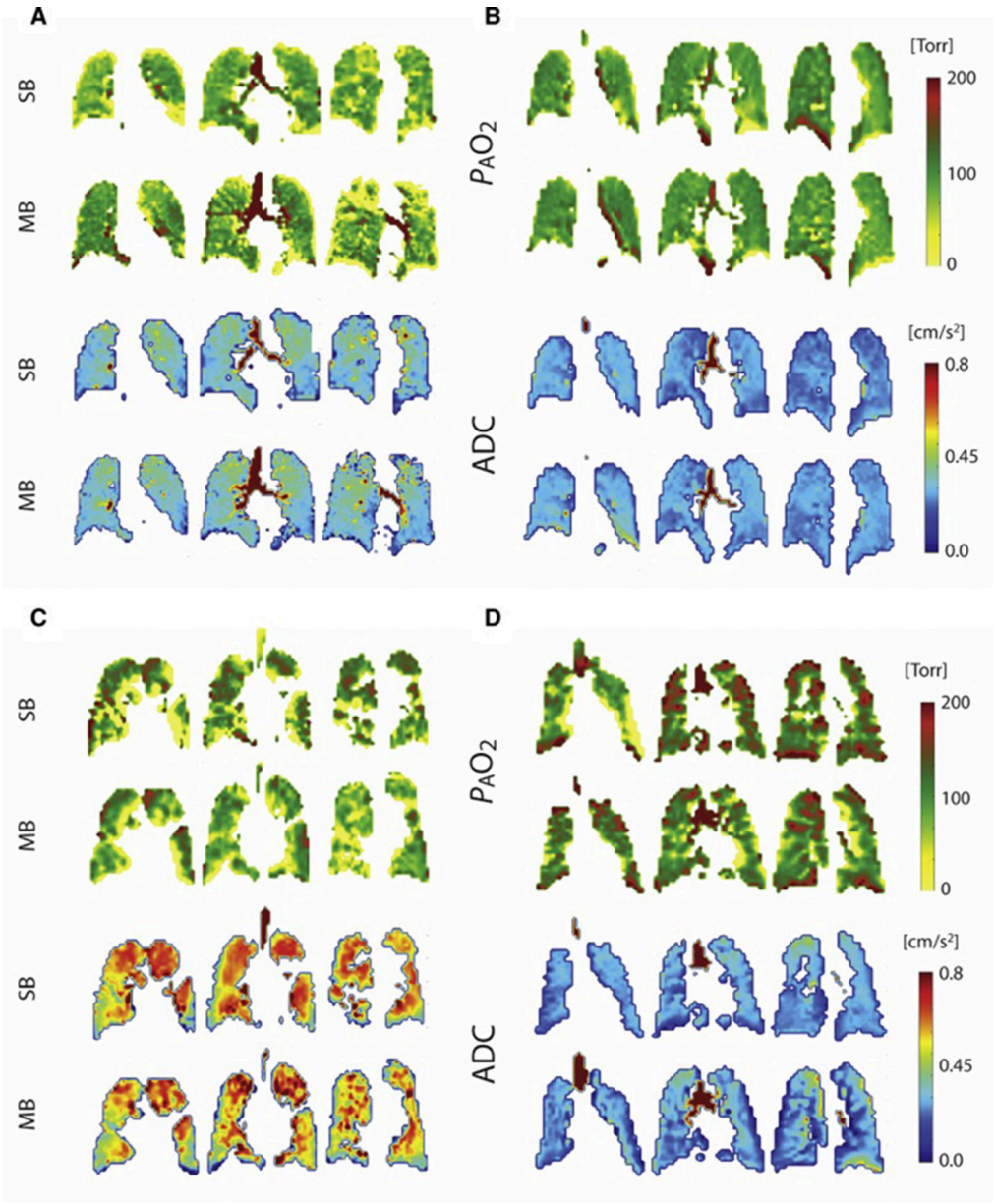

Figure 5).

PAO2 maps (top) and ADC maps (bottom) in four representative subjects (clockwise from top left: AS3: Age 67 yrs., FEV1/FVC: 72%; AS4: Age: 62 yrs., FEV1/FVC: 77; COPD1: Age 70 yrs., FEV1/FVC: 35%; COPD5: Age: 61 yrs; FEV1/FVC: 49%).

In the PAO2 maps, the color scale differentiates regions of abnormally high PAO2 values, which may correlate with slow-filling regions, from those with abnormally low PAO2 values, which may correlate with over-inflation and subsequent loss of signal intensity through resolution of pressure gradients. In the ADC maps, the color scale highlights regions of extremely high diffusion, which could be indicative of emphysema.

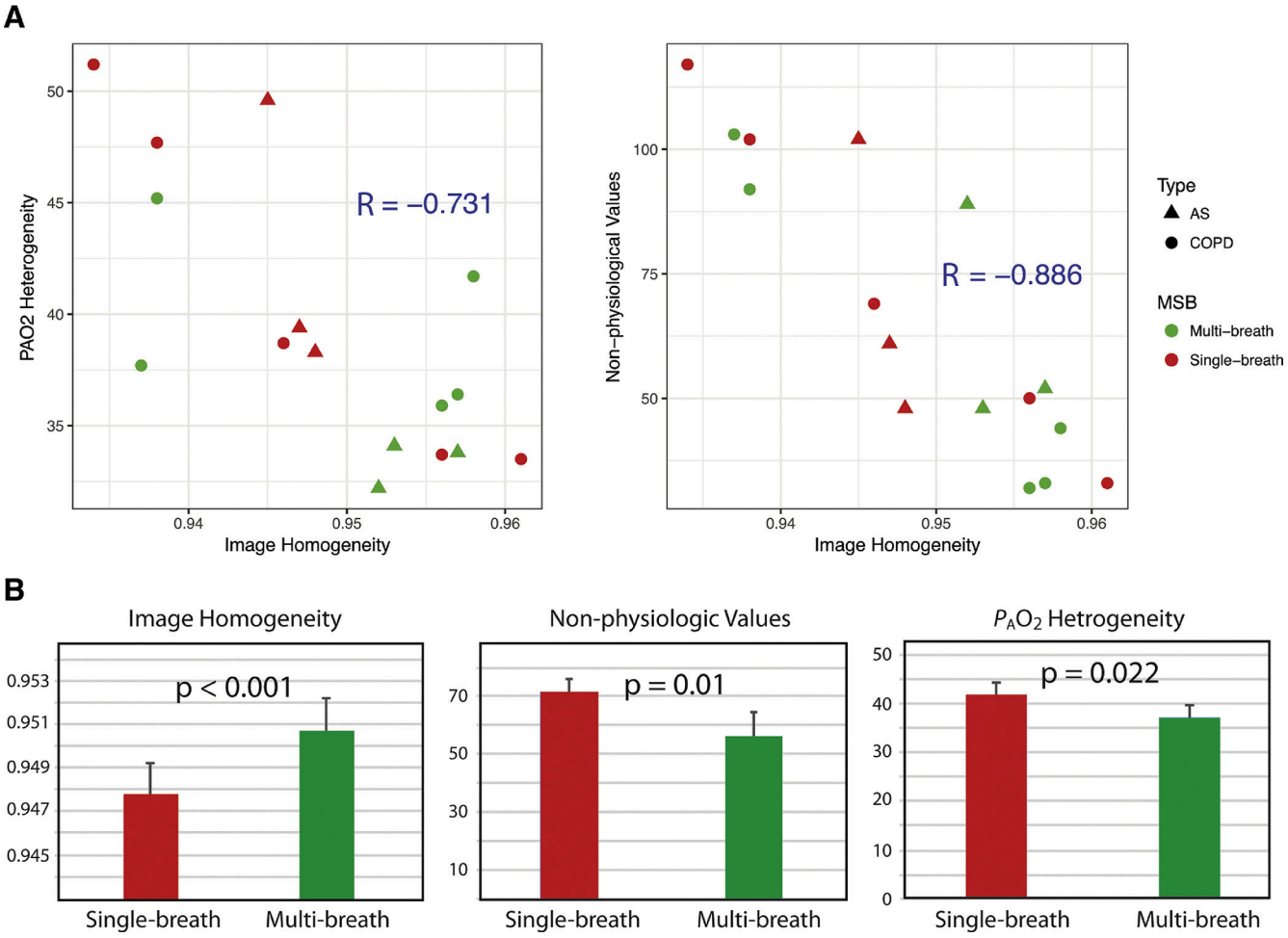

Figure 6).

Image (spin density) homogeneity, as calculated from the homogeneity marker (refer to methods), plotted against P_AO_2 heterogeneity (a, left). Image homogeneity plotted against the number of non-physiological values (a, right). Bar graphs comparing image homogeneity, non-physiologic values, and P_AO_2 heterogeneity in single-breath versus multi-breath imaging.

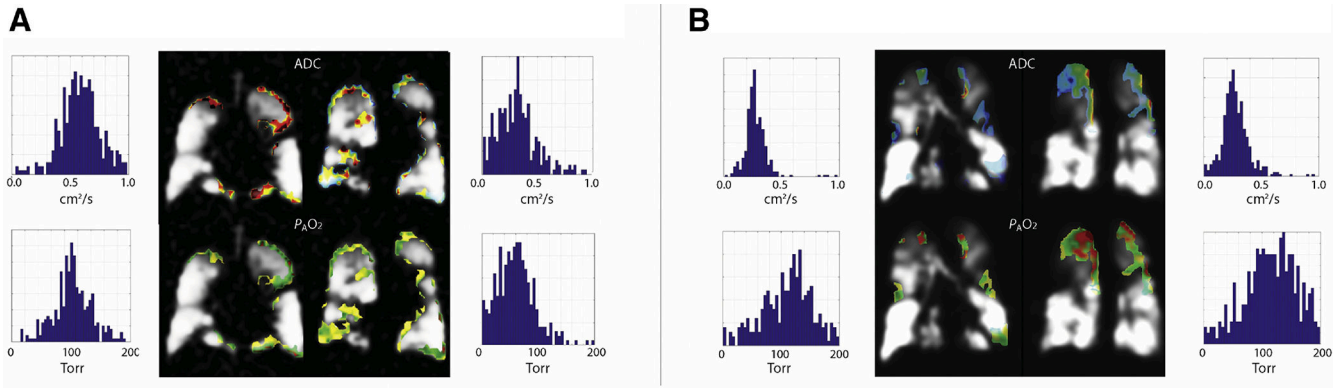

Figure 7).

Spin density maps from representative subjects COPD 1: Age 70 yrs., BMI: 27.2, FEV1/FVC: 0.35, DLCO: 37% Pred., RV/TLC: 62% (A) and COPD 5: Age: 61 yrs., BMI: 23.7, FEV1/FVC: 49%, DLCO: 51% Pred., RV/TLC: 59% (B). ADC and PAO2 color maps are overlaid on the regions identified as slow-filling – regions that were not filled with ^{3}He gas in the single-breath protocol, but are filled under the multi-breath method. Histograms are also included for each slice, including ADC value versus incidence (top) and PAO2 value versus incidence (bottom).

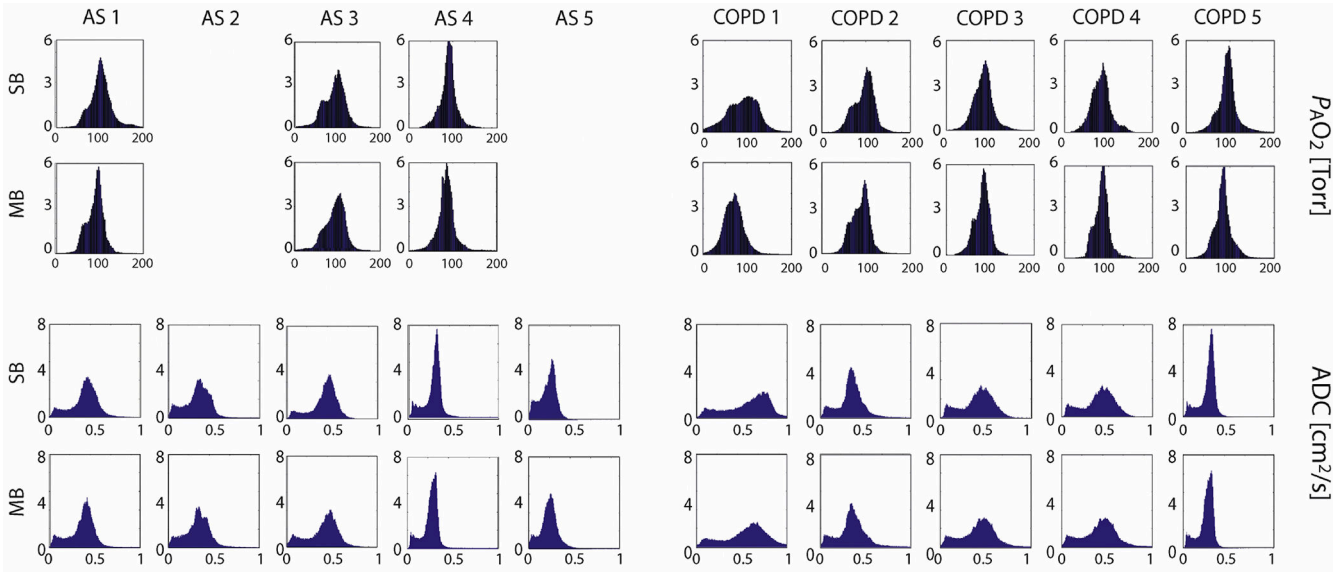

Figure 8).

Top: histogram distributions of P_AO_2 values from single-breath imaging (top) and multi-breath imaging (bottom) from all subjects. **Bottom:** histogram distributions of ADC values from single-breath imaging (top) and multi-breath imaging (bottom) versus.

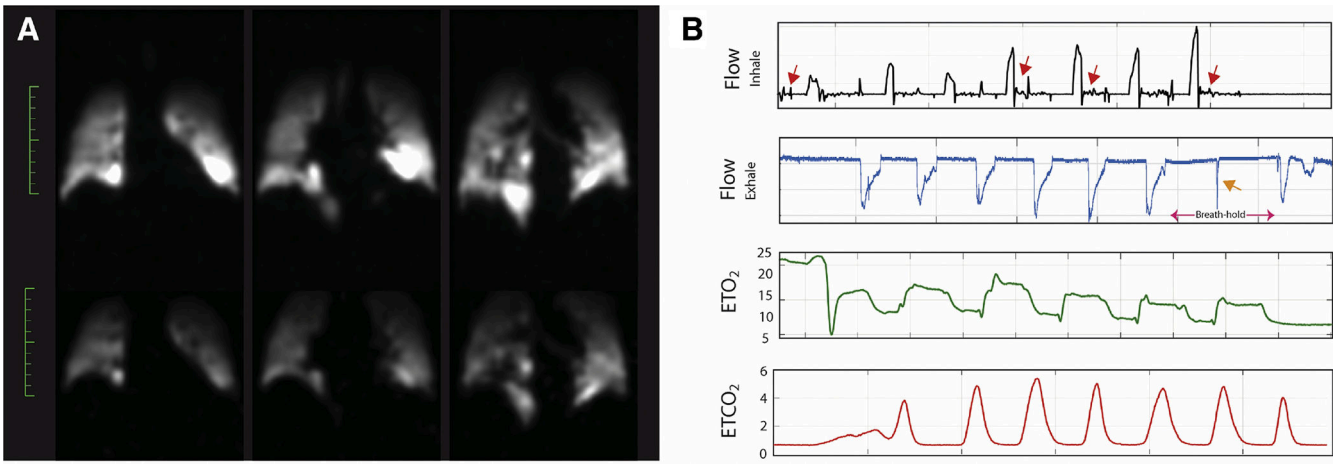

Figure 9).

A: Spin–density maps for the case of a representative subject who exhaled in the middle of the breath-hold. **B:** Gas delivery monitoring system plots indicating (from top to bottom) the flow of inhaled gas (black graph), flow of exhaled gas (blue graph), End-tidal O_2 (green graph; EtO_2) and End-tidal CO_2 (red graph; $EtCO_2$) from different representative subjects to indicate the cases in which the breathing protocol was not followed properly. The red arrows in the top plot indicate intermittent inhalation attempts during the breath-hold, while the orange arrows on the second from top graph shows the exhalation during the breath-hold.

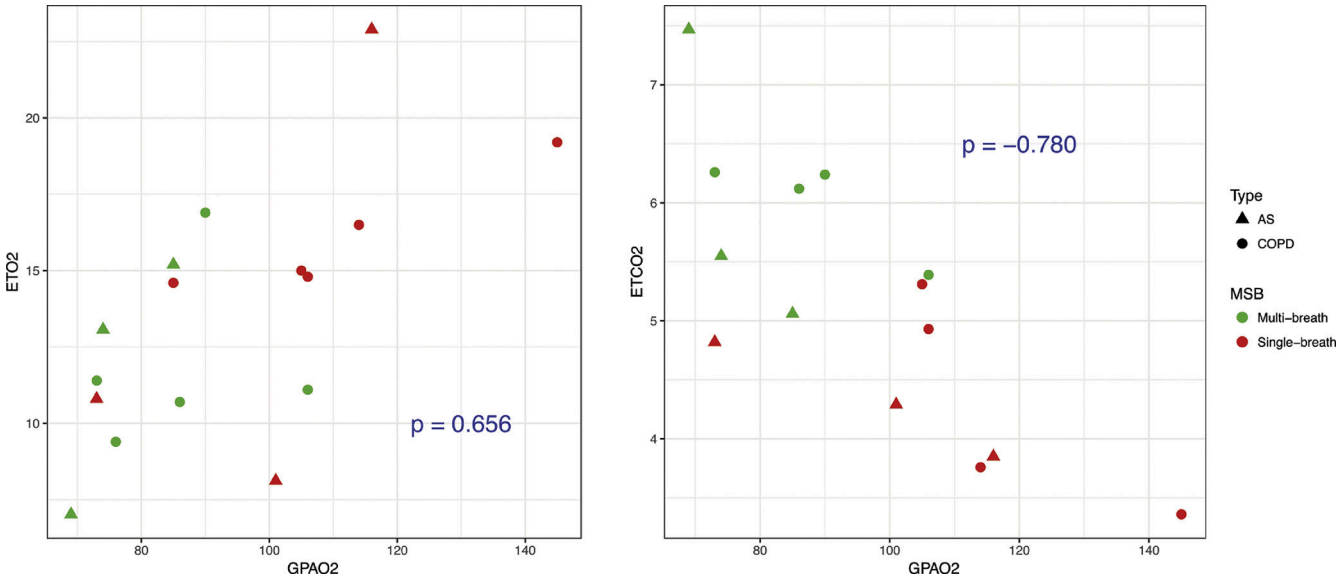

Figure 10).

Scatter-plots of expired O_2 (EtO_2) (left) and expired CO_2 (ECO_2) (right) collected from both COPD and AS cohorts against their global P_AO_2 values.

TABLE 1.

Demographics and a Subset of Clinical Test Results

Subject	Demographics					PFTs						
	Age (Years)	TLC (L)	Height (in)	Weight (lb)	BMI (kg/m^2)	FEV_1 (L)	FEV_1/FVC (%)	RV/PLC (%)	DL_{CO}(mL/min/mmHg)	Pred. FEV_1 (%)	Pred. DL_{CO} (%)	Life Impact SGRQ Overall (%)
AS 1	58	6.01	64.5	141.7	23.9	2.97	78	34	19.29	117	91	15.9
AS 2	64	5.95	70.5	167	23.6	2.88	71	32	19.75	93	88	6.51
AS 3	67	6.91	66.5	198	31.5	2.81	72	46	23.73	110	93	29
AS 4	62	6.55	71.5	176	23.9	3.01	77	36	33.46	80	127	10.39
AS 5	31	7.87	75	207	25.9	5.19	80	16	34.2	101	92	2.64
Mean ± SD	56.4 ± 13.03	6.66 ± 0.79	69.6 ± 3.72	177.9 ± 23.2	25.76 ± 2.98	3.37 ± 0.91	75.6 ± 3.50	32.8 ± 9.68	26.09 ± 6.51	100.2 ± 12.95	98.2 ± 14.50	12.89 ± 9.17
COPD 1	70	6.57	69	184	27.2	0.88	35	59	8.7	28	37	51.5
COPD 2	68	5.04	63.5	158.5	27.2	1.54	58	46	12.44	83	73	18.88
COPD 3	60	9.24	67	178	27.9	1.26	40	62	14.66	39	59	29.79
COPD 4	55	5.14	67	180	28.2	2.29	71	41	16.07	92	68	57.16
COPD 5	61	3.71	63	134	23.7	0.67	49	62	8.95	27	51	7.727
Mean ± SD	62.8 ± 6.14	5.94 ± 2.10	65.9 ± 2.56	166.9 ± 20.9	26.84 ± 1.81	1.33 ± 0.63	51.8 ± 16.6	54.0 ± 9.82	12.16 ± 3.31	53.8 ± 31.28	57.6 ± 14.28	33.01 ± 21.06
P (T ≤ t)	0.406	0.542	0.268	0.587	0.548	0.036	0.036	0.038	0.014	0.080	0.006	0.088

BMI, body mass index; COPD, chronic obstructive pulmonary disease; SD, standard deviation; SGRQ, St. George's Respiratory Questionnaire.

TABLE 2.

Imaging Markers

	P_AO_2						ADC			
	Single-breath			Multibreath			Single-breath		Multibreath	
Subject	**Global (Torr)**	**Heterogeneity* (Torr)**	**<40 or >160 Nonphysiol.†**	**Global (Torr)**	**Heterogeneity* (Torr)**	**<40 or >160 Nonphysiol.†**	**Global (cm^2/s)**	**Heterogeneity* (cm^2/s)**	**Global (cm^2/s)**	**Heterogeneity* (cm^2/s)**
AS 1	116	43	61	69	35	52	0.356	0.118	0.391	0.097
AS 2‡	-	-	-	-	-	-	0.315	0.106	0.317	0.124
AS 3	73	42	102	85	36	89	0.320	0.109	0.328	0.108
AS 4	101	35	48	74	34	48	0.263	0.072	0.272	0.070
AS 5 ‡	-	-	-	-	-	-	0.204	0.099	0.205	0.111
Mean ± SD	97 ± 22	40 ± 4	70 ± 28	76 ± 8	35 ± 1	63 ± 23	0.292 ± 0.059	0.101 ± 0.017	0.303 ± 0.069	0.102 ± 0.02
COPD 1	106	49	117	73	36	103	0.547	0.143	0.598	0.157
COPD 2	105	42	69	86	34	44	0.396	0.109	0.414	0.119
COPD 3	114	39	33	90	33	33	0.328	0.107	0.329	0.124
COPD 4	85	38	50	76	30	32	0.396	0.111	0.402	0.135
COPD 5	145	48	101	106	42	92	0.269	0.072	0.264	0.119
Mean ± SD	111 ± 22	43 ± 5	67 ± 44	86 ± 13	35 ±4	56 ± 41	0.387 ± 0.104	0.108 ± 0.025	0.401 ± 0.125	0.131 ± 0.016
P (T ≤ t)	0.416	0.367	0.877	0.225	0.384	0.916	0.122	0.609	0.172	**0.037**

ADC, apparent diffusion coefficient; COPD, chronic obstructive pulmonary disease; SD, standard deviation.

*Standard deviation.

†Number of voxels with nonphysiologic values.

‡The subject is excluded in statistical comparisons due to failed breathing protocol.

Table 3-

Imaging Markers

		Slow-filling Voxels			
	VDV	ADC		P_AO_2	
Subject	Decrease [%]	Mean [Torr]	SD [Torr]	Mean [cm ^{2} /s]	SD [cm ^{2} /s]
AS 1	15.8	0.372	0.267	59.8	22.0
AS 2	5.7	0.323	0.054	-	-
AS 3	13.6	0.274	0.093	73.6	26.4
AS 4	11.2	0.296	0.083	66.4	19.2
AS 5	3.5	0.206	0.033	-	-
mean ± sd	10 ± 6.2	0.314 ± 0.052	0.147 ± 0.103	66.6 ± 6.9	22.5 ± 3.6
COPD 1	24.7	0.610	0.237	88.0	30.8
COPD 2	8.2	0.426	0.163	59.7	29.2
COPD 3	14.5	0.337	0.076	109.6	28.6
COPD 4	10.3	0.419	0.047	86.1	21.5
COPD 5	21.0	0.244	0.036	98.4	26.1
mean ± sd	15.7 ± 7	0.455 ± 0.14	0.12 ± 0.103	88.4 ± 18.6	27 ± 4.9
P(T<=t)	0.180	0.144	0.922	0.060	0.144